Active Optical Metasurfaces Based on Defect-Engineered Phase-Transition Materials

NANO LETTERS

Letter

pubs.acs.org/NanoLett

Active Optical Metasurfaces Based on Defect-Engineered Phase-Transition Materials

Jura Rensberg,[*,†] Shuyan Zhang,[‡] You Zhou,[‡] Alexander S. McLeod,[§] Christian Schwarz,[†] Michael Goldflam,[§] Mengkun Liu,[§,∥] Jochen Kerbusch,[⊥] Ronny Nawrodt,[†] Shriram Ramanathan,[‡,#] D. N. Basov,[§] Federico Capasso,[‡] Carsten Ronning,[†] and Mikhail A. Kats[*,‡,∇,○]

[†]Institute for Solid State Physics, Friedrich-Schiller-Universität Jena, 07743 Jena, Germany

[‡]John A. Paulson School of Engineering and Applied Sciences, Harvard University, Cambridge, Massachusetts 02138, United States

[§]Department of Physics, University of California - San Diego, La Jolla, California 92093, United States

[∥]Department of Physics, Stony Brook University, Stony Brook, New York 11794, United States

[⊥]Institute of Ion Beam Physics and Materials Research, Helmholtz-Zentrum Dresden-Rossendorf, 01328 Dresden, Germany

[#]School of Materials Engineering, Purdue University, West Lafayette, Indiana 47907, United States

[∇]Department of Electrical and Computer Engineering and [○]Materials Science Program, University of Wisconsin - Madison, Madison, Wisconsin 53706, United States

Supporting Information

ABSTRACT: Active, widely tunable optical materials have enabled rapid advances in photonics and optoelectronics, especially in the emerging field of meta-devices. Here, we demonstrate that spatially selective defect engineering on the nanometer scale can transform phase-transition materials into optical metasurfaces. Using ion irradiation through nanometer-scale masks, we selectively defect-engineered the insulator-metal transition of vanadium dioxide, a prototypical correlated phase-transition material whose optical properties change dramatically depending on its state. Using this robust technique, we demonstrated several optical metasurfaces, including tunable absorbers with artificially induced phase coexistence and tunable polarizers based on thermally triggered dichroism. Spatially selective nanoscale defect engineering represents a new paradigm for active photonic structures and devices.

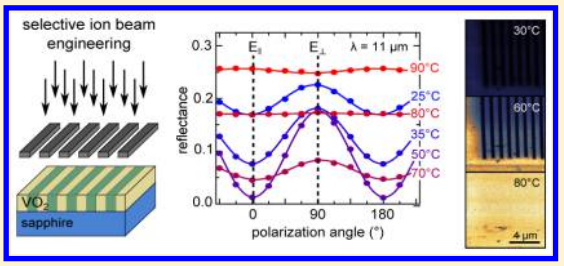

KEYWORDS: *Metasurfaces, metamaterials, meta-devices, defect engineering, phase-transition materials*

Tunable optical metamaterials and metasurfaces are an emerging frontier with promising applications including optical modulation, routing, dynamic beam shaping, and adaptive optics.[1−5] Dynamic control in meta-devices can be achieved by careful integration of existing designs with active media, for example, liquid crystals,[6,7] graphene,[8] or strongly electron-correlated[9−11] and chalcogenide[12] phase-transition materials. Phase-transition materials featuring various structural and electronic transitions such as germanium antimony tellurium (GST),[12−14] vanadium dioxide (VO_2),[9,15−17] and rare-earth nickelates[18] have particular promise because of their large change of optical properties given an applied stimulus compared to, for example, Kerr materials[19] or liquid crystals.[6,7,20] Of the phase-transition materials, one of the most prolifically studied is VO_2, which exhibits a reversible insulator-metal transition (IMT) as the temperature reaches a critical temperature $T_C \sim 67$ °C.[17] This transition, which takes VO_2 from its low-temperature insulating monoclinic phase to the high-temperature metallic rutile phase, corresponds to a resistivity change of up to up to 5 orders of magnitude and a dramatic change in the complex refractive index, especially at infrared (IR) wavelengths.[21] Here we describe how ion beam irradiation[22] can be used to modify and engineer the thermally driven IMT of vanadium dioxide via the intentional creation of structural defects and lattice damage ("defect engineering"). Unlike existing means to modify the IMT via doping during growth,[23] ion beam irradiation can be combined with lithographic patterning to create complex optical meta-devices with designer phase transitions (Figure 1).

The insulating phase of VO_2 is a Mott-Peierls insulator with both electron-electron correlations and dimerization of vanadium ions contributing to the opening of an insulating gap.[24] Thus, the IMT is very sensitive to the stability of the electron hybridization and therefore to electronic doping,[23] structural defects,[25,26] and lattice strain,[27−29] all of which can be introduced via ion beam irradiation. To investigate the effect of the irradiation on the optical properties, we performed temperature-dependent near-infrared transmittance measure-

Received: October 9, 2015
Revised: December 16, 2015
Published: December 21, 2015

DOI: 10.1021/acs.nanolett.5b04122
Nano Lett. 2016, 16, 1050−1055

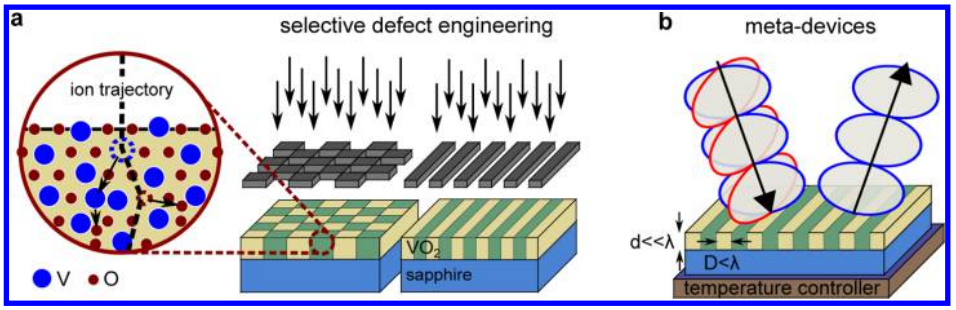

Figure 1. Optical meta-devices based on defect engineering of phase-transition materials. (a) The thermally driven insulator-to-metal phase transition of vanadium dioxide (VO_2) can be modified by deliberately introducing structural defects into the lattice (defect engineering). Spatially selective defect engineering is achieved by ion beam irradiation through a mask. The enlarged area shows the primary displacement of both vanadium and oxygen lattice atoms by an incoming energetic ion and the subsequent damage cascade. The complex refractive indices of the insulating and metallic states are similar for the intrinsic and irradiated VO_2, but the phase transition of the irradiated regions occurs at a much lower temperature (see also Supporting Information S5). (b) The irradiated features can be made much smaller than the wavelength of light, so the resulting film becomes a metasurface with effective optical properties. One example is a tunable polarizer comprising stripes of irradiated and intrinsic VO_2, creating a metasurface with a variable degree of optical anisotropy.

ments (λ = 2.5 μm) of intrinsic and irradiated VO_2 films (Figure 2). The highly oriented epitaxial VO_2 films were grown

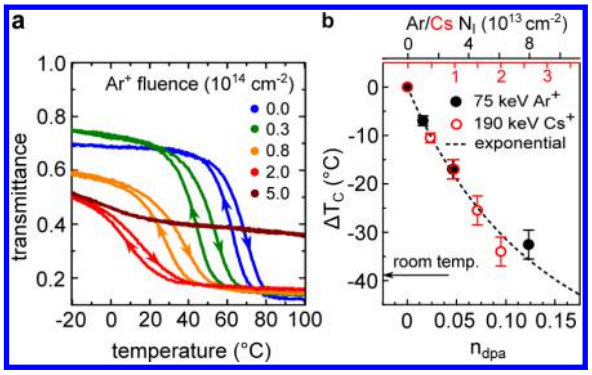

Figure 2. Defect engineering via ion beam irradiation. (a) Temperature-dependent transmittance (λ = 2.5 μm) of a 100 nm VO_2 film on *c*-plane sapphire irradiated with 75 keV Ar^+ ions for various ion fluences. The arrows mark the heating and cooling branches of the hysteresis curves. (b) Experimentally determined shift of the phase transition temperature (ΔT_C) versus the calculated n_{dpa}, given irradiation with 75 keV Ar^+ and 190 keV Cs^+ ions. The energy, mass, and fluence of the ion irradiation determine the n_{dpa}. The data points for Ar^+ and Cs^+ fall on the same curve and, because argon is not incorporated into the VO_2 lattice, we conclude that the shift of the critical temperature is a result of lattice defects induced by ion irradiation and is not caused by impurity doping. The exponential curve is a common fit to both sets of points using a direct impact damage formation model (Supporting Information S3).

to a thickness of ~100 nm on *c*-plane sapphire and then irradiated with varying fluences of 75 keV Ar^+ ions, corresponding to a Gaussian depth profile centered at the middle of the film (see Supporting Information Methods and Supporting Information S1–S4). Argon was chosen because it is a noble gas and is thus not chemically incorporated in the VO_2 lattice, enabling the study of the effects of irradiation-induced lattice defects separate from any impurity doping. The transmittance of all films decreased with increasing temperature (Figure 2a), a result of increasing free carrier concentration during the transition from the insulating to the metallic state, and displayed a hysteresis loop that is characteristic of a first-order phase transition.[30] We calculated the critical temperature T_C of the IMT as the average of the temperatures of the largest slope of the transmittance versus temperature curves for the heating and cooling cycles, respectively.[31]

When the films were irradiated with an increasing Ar^+ ion fluence N_I (number of ions per unit area), the transition temperature decreased, reaching room temperature for $N_I \sim 1 \times 10^{14}$ cm^{-2} (Figure 2a,b). This effect is a result of irradiation damage, that is, the displacements of both oxygen and vanadium from their lattice sites by nuclear collisions that lead to the formation of stable interstitial-vacancy complexes (Frenkel pairs) at low ion fluences,[32] reducing T_C via the local compressive strain[27,28] induced in the lattice by atomic displacements.[33] We attribute the broadening of the transition width for increasing ion fluences to the Gaussian depth distribution of lattice defects, and the reduction of transmittance in the insulating state (Figure 2a) to absorption within the band gap resulting from the increasing number of defect states. For the highest ion fluences (>5 × 10^{14} cm^{-2}), the accumulation of point defects leads to the formation of amorphous regions of VO_2 that overlap until a continuous amorphous VO_2 film is formed (see Supporting Information S3). For a comparable shift of T_C to room temperature by ion beam impurity doping with tungsten, the most efficient dopant,[23] $N_I \sim 10^{16}$ cm^{-2} would be necessary, far above the amorphization threshold. Amorphous films of VO_2 do not feature an IMT.[34]

To confirm that the shift of T_C (ΔT_C) is caused by irradiation damage rather than impurity doping or stress from the impurity atoms themselves, we repeated the experiment with 190 keV Cs^+ ions, which have a much larger ionic radius (Figure 2b). The energy was chosen to ensure an implantation profile comparable to that of the Ar^+ irradiation (see Supporting Information S2). To compare ΔT_C induced by the same density of lattice defects due to Ar^+ and Cs^+ ion irradiation, respectively, we estimated the fraction of atoms that have been displaced by the incoming ions (number of primary displacements per lattice atom, n_{dpa}) (see Supporting Information Methods). T_C is found to be roughly independent of the ion species, depending only on n_{dpa}, and reaches room temperature when less than ~15% of all lattice atoms are displaced (Figure 2b). The irradiation defects are stable in the temperature range investigated in this work and remain unaltered after many cycles through the IMT (Supporting Information S8). Thus, we can conclude that defect engineering

DOI: 10.1021/acs.nanolett.5b04122
Nano Lett. 2016, 16, 1050–1055

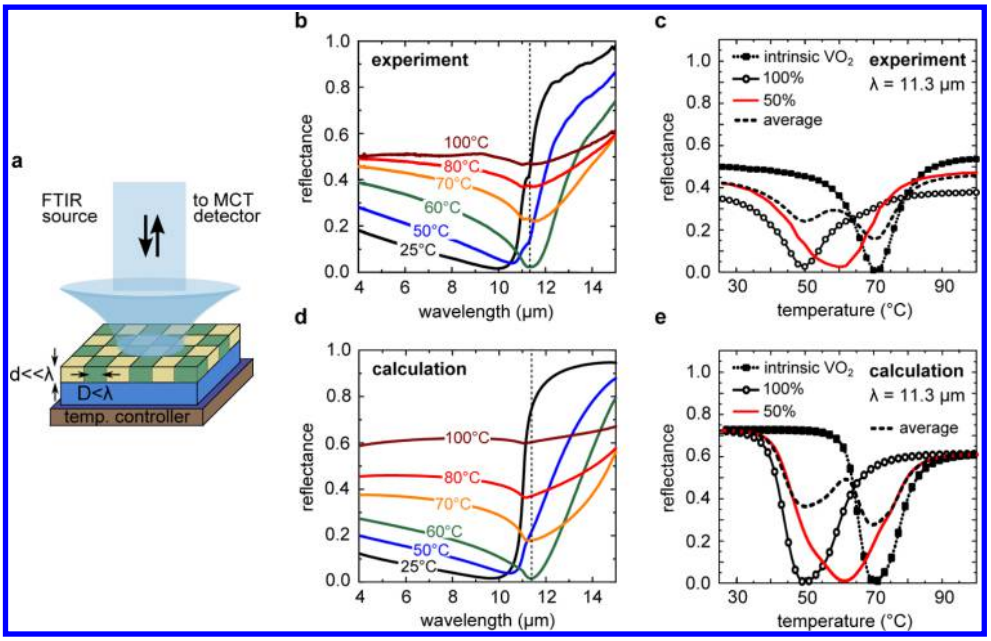

Figure 3. Artificially induced persistent phase coexistence. (a) Schematic drawing of the near-normal incidence reflectance measurement using an infrared microscope and a temperature-controlled stage. (b) Temperature-dependent reflectance of the checkerboard structure (area coverage D = 50%, period = 500 nm, film thickness = 100 nm). At a critical temperature, the reflectance of the sample drops to almost zero for λ = 11.3 μm due to an ultrathin film interference interaction between the film and the substrate.[35] (c) Measured reflectance of intrinsic, checkerboard structure (D = 50%), and completely irradiated (D = 100%) films at λ = 11.3 μm. The subwavelength checkerboard structure possesses effective optical properties that cannot be trivially deduced by averaging the reflectance of the intrinsic and fully irradiated samples (dashed line), and appears to have a single broadened phase transition. (d,e) Calculated reflectance for the sample measured in (b,c) using Fresnel equations and our effective medium approximation (see Supporting Information S6 and S7).

using ion irradiation with various ions can be used to broadly tune the critical temperature of the IMT.

The IMT in VO_2 is particularly useful for tunable optical and optoelectronic devices because it occurs gradually over a range of temperatures and provides access to a wide range of complex refractive index values.[15,35,36] At the onset of the IMT, nanoscale islands of the metallic phase start to nucleate surrounded by insulating VO_2, which then grow and connect in a percolation process.[15] Because of this phase coexistence on a subwavelength scale, VO_2 in its transition region has been described as a natural disordered optical metamaterial.[36] A similar gradual refractive index change can be observed in GST.[37] However, it has been noted that the intrinsic transition temperature of VO_2 limits the utility of this material for devices.[12] Now using area-selective defect engineering with ion fluences significantly smaller than the amorphization threshold of VO_2, we can obtain control over the shape, temperature, and persistence of the phase coexistence regions by selectively irradiating appropriate regions of the VO_2 film, locally modifying the IMT (Figure 1). In the temperature range where irradiated VO_2 regions are metallic while the intrinsic regions are insulating, persistent phase coexistence of metallic and insulating domains with a fixed metallic fraction is artificially induced.

We fabricated a sample composed of defect-engineered and intrinsic VO_2 regions in a square checkerboard arrangement (period = 0.5 μm) by irradiating a 100 nm VO_2 film on c-plane sapphire with 190 keV Cs^+ through a poly(methyl methacrylate) (PMMA) mask made using electron-beam lithography (Figures 1a and 3a). The ion fluence was set to $N_I = 1 \times 10^{13}$ cm^{-2}, which corresponds to n_{dpa} = 0.05 (i.e., 5% of all lattice atoms are displaced), and decreases T_C of the irradiated region to ~50 °C (Figure 2b). We probed the temperature-dependent effective optical properties of this sample via mid-IR reflectance measurements using a Fourier transform infrared (FTIR) spectrometer and a mid-IR microscope (Figure 3). The mid-IR was chosen because the carrier concentration change due to the IMT leads to greater changes of the refractive index compared to the visible and near-infrared.

At low temperatures, both the irradiated and intrinsic VO_2 regions are insulating and essentially transparent. The reflectance spectrum is dominated by the onset of a prominent Reststrahlen band of the sapphire substrate, leading to high reflectivity above ~11 μm. As the temperature T is increased, the mid-IR reflectance changes monotonically in the 4−10 μm region and nonmonotonically in the 10−15 μm region, reaching a minimum-reflectance point at λ = 11.3 μm and T_{min} = 60 °C. Such a reflectance minimum is also found in the vicinity (~3 °C below) of the phase transition at a metallic fraction of ~33% in intrinsic and fully irradiated samples (Figure 3c, also see Supporting Information S5 and S6) and is a result of an "ultrathin-film interference condition" found in highly absorbing films on certain reflective substrates.[35] Note that for sapphire, the wavelength at which this reflectance minimum appears is fixed to a relatively narrow range within the Reststrahlen band, where the complex refractive index is similar to that of metals at visible or UV frequencies and can be tuned slightly by the film thickness.[35] Comparable complex refractive indices can also be found in a variety of other substrates in the visible and mid-IR, for instance, highly doped semiconductors and transparent conducting oxides.[36]

In particular, the reflectance of the sample at λ = 11.3 μm as a function of temperature (Figure 3c) shows that the subwavelength checkerboard structure possesses effective optical properties that cannot be trivially deduced by averaging the reflectance of the intrinsic and fully irradiated samples.

DOI: 10.1021/acs.nanolett.5b04122
Nano Lett. 2016, 16, 1050−1055

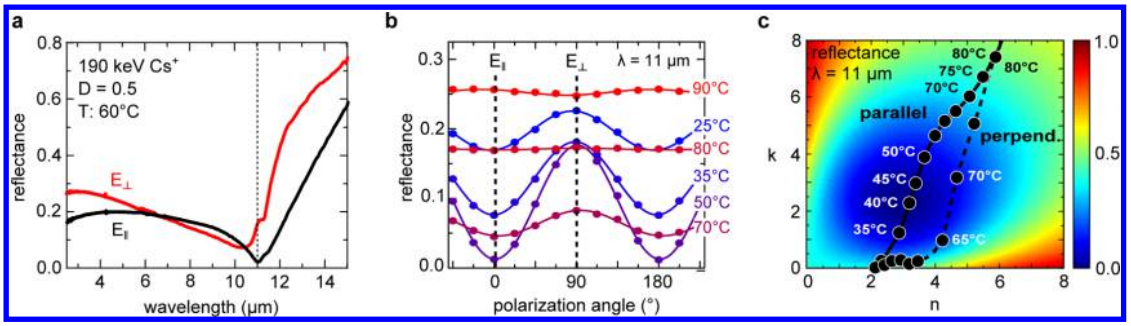

Figure 4. Switchable polarizer via tunable anisotropy. (a) Measured reflectance of the anisotropic metasurface shown in Figure 1b, comprised of stripes of irradiated and intrinsic VO_2 (film thickness = 100 nm, D = 50%, period = 1000 nm) on a sapphire substrate. The sample temperature was maintained at 60 °C, between the transition temperatures of the intrinsic and irradiated VO_2, for light polarized parallel ($E_\parallel$) and perpendicular ($E_\perp$) to the ridges. Light polarized parallel to the ridges is preferentially absorbed at $\lambda \sim 11$ μm. (b) Evolution of the polarization-dependent reflectance at $\lambda = 11$ μm for increasing temperatures between 25 and 90 °C. (c) Calculated map of the reflectance at $\lambda = 11$ μm as a function of the real and imaginary part of the complex refractive index $\tilde{n} = n + ik$ of an arbitrary 100 nm film on sapphire. The lamellar grid pattern is equivalent to a uniaxial crystal with form birefringence and dichroism. The solid (dashed) line marks the calculated temperature-dependent complex refractive index of a patterned VO_2 film for light that is polarized parallel (perpendicular) to the ridges.

While the reflectance minimum of irradiated and intrinsic VO_2 regions occurs independently at ~50 and ~70 °C and has a full width at half-minimum (FWHM) of ~15 and ~12 °C, respectively, the subwavelength checkerboard appears to have a single effective reflectance minimum at ~60 °C with a FWHM >25 °C.

Because of the subwavelength nature of the checkerboard ("check") pattern features, we can treat the patterned VO_2 film as an effective medium that has a well-defined temperature- and wavelength-dependent complex refractive index

$$\tilde{n}_{\text{eff}}^{\text{check}}(T) = \sqrt{\tilde{n}_{\text{int}}(T)\tilde{n}_{\text{irr}}(T)} \quad (1)$$

where $\tilde{n}_{\text{int}}(T)$ and $\tilde{n}_{\text{irr}}(T)$ are the temperature-dependent refractive indices of intrinsic and irradiated VO_2 regions, calculated from the refractive indices of insulating and metallic VO_2, extracted from the measurements of Quazilbash et al.[15] using the Bruggeman equation (see Supporting Information S6 and S7). Taking into account the effective optical constants, we used Fresnel equations to calculate the reflectance of the samples (Figure 3d, e, Supporting Information S6), which are in agreement with the measurements. Differing absolute reflectance values are most likely due to both a different optical quality of our intrinsic VO_2 sample compared to that in ref 15, and an increasing amount of lattice defects after ion irradiation.

Our results show that the temperature range of phase coexistence can be greatly increased by patterned ion irradiation, because the metallic fraction will remain roughly constant in the temperature range between the transition temperatures of the irradiated and intrinsic VO_2 regions (e.g., between 50 and 70 °C in Figure 3c). Furthermore, the metallic fraction can be adjusted by changing D. The optical properties can then be tuned in and out of an artificially designed effective medium state over a desired range of temperatures. We note that a vertical (rather than lateral) distribution of phase transition temperatures has been achieved in thin VO_2 films synthesized from colloidal VO_x nanocrystal solutions with various tungsten doping densities.[38]

Further functionality can be achieved by realizing VO_2-based anisotropic metasurfaces with tunable dichroism. Anisotropic phase coexistence in thin VO_2 films has been observed on TiO_2 substrates and occurs naturally due to strain[39] but requires particular substrates and provides little control over the degree of anisotropy. Similar phase coexistence was also achieved by selective laser heating of embedded VO_2 nanoparticles, though this structure is not temperature tunable.[40]

We fabricated a periodic structure consisting of parallel ridges with a width of 0.5 μm and a period of 1 μm by irradiating a suitably masked sample with 190 keV Cs^+ ions at a fluence of $N_I = 2 \times 10^{13}\text{cm}^{-2}$, corresponding to $n_{dpa} = 0.09$ (compare also Figure 1a). At a temperature where only the irradiated VO_2 is metallic, the reflectance from the patterned region is polarization-dependent over most of the $\lambda = 2-15$ μm wavelength region, indicating a large degree of dichroism (Figure 4a, b). Especially at the wavelength at which minimal reflection occurs ($\lambda = 11$ μm in Figure 4a), light polarized parallel to the ridges ($E_\parallel$) is preferentially absorbed.

Figure 4b shows the measured polarization-dependent reflectance at $\lambda = 11$ μm as a function of increasing temperature. The reflectance is small from 40 to 70 °C for light polarized parallel to the ridges ($E_\parallel$), and a value of $R_\parallel \sim 0.01$ is reached at $T \sim 50$ °C. At the same temperature, the reflectance for the orthogonal polarization is $R_\perp = 0.17$. As a consequence, unpolarized light reflected from the patterned VO_2 film becomes highly polarized with a degree of linear polarization (DOLP) of ~90%, defined as intensity of light reflected with the preferential polarization minus the intensity of light reflected perpendicular to it divided by the sum of both.[41] The polarization dependence vanishes above 75 °C, as both regions become metallic. Therefore, our device can be tuned in and out of the highly polarizing state by tuning the temperature.

To better understand the temperature- and polarization-dependent reflectance, we calculated the reflectance of a 100 nm thick anisotropically patterned VO_2 film on sapphire for normally incident light that is polarized parallel (∥) or perpendicular to the ridges (⊥), respectively. When the wavelength is large enough, the refractive indices for a periodic structure consisting of ridges can be expressed as[42]

$$\tilde{n}_{\parallel}^{\text{grid}}(T) = [(1-D)\tilde{n}_{\text{int}}^2(T) + D\tilde{n}_{\text{irr}}^2(T)]^{1/2} \quad (6)$$

$$\tilde{n}_{\perp}^{\text{grid}}(T) = \frac{[\tilde{n}_{\text{int}}(T)\tilde{n}_{\text{irr}}(T)]}{[D\tilde{n}_{\text{int}}^2(T) + (1-D)\tilde{n}_{\text{irr}}^2(T)]^{1/2}} \quad (7)$$

D is the area coverage (duty cycle) of the irradiated VO_2 and $\tilde{n}_{\text{int}}(T)$ and $\tilde{n}_{\text{irr}}(T)$ are the temperature-dependent refractive

DOI: 10.1021/acs.nanolett.5b04122
Nano Lett. 2016, 16, 1050−1055

indices of intrinsic and irradiated VO_2 regions (see Supporting Information S6 and S7). The calculated complex refractive index trajectories are plotted in Figure 4c onto the *n*-*k* space map of calculated reflectance for a 100 nm thin film of arbitrary refractive index on sapphire at λ = 11 μm (see Supporting Information S6). At the lowest (<25 °C) and the highest (>70 °C) temperatures, the refractive index values for parallel and perpendicular polarized light are the same, whereas for all intermediate temperatures they differ because of the induced anisotropy (eqs 6 and 7). In this temperature region, the complex refractive index change in the mid-infrared is much greater than 1, whereas typical values achievable using, for example, the Kerr effect are no greater than $\sim 10^{-4}$.[43] The predicted DOLP is 98% and can be improved to almost 100% by choosing an appropriate film thickness.

Although far-field measurements can probe the effective optical properties, the subwavelength patterns of irradiated VO_2 cannot be resolved due to the diffraction limit. To explore the limits of our approach such as the sharpness of the boundary between irradiated and intrinsic areas, we performed near-field imaging (Figure 5). Mid-infrared near-field images at different

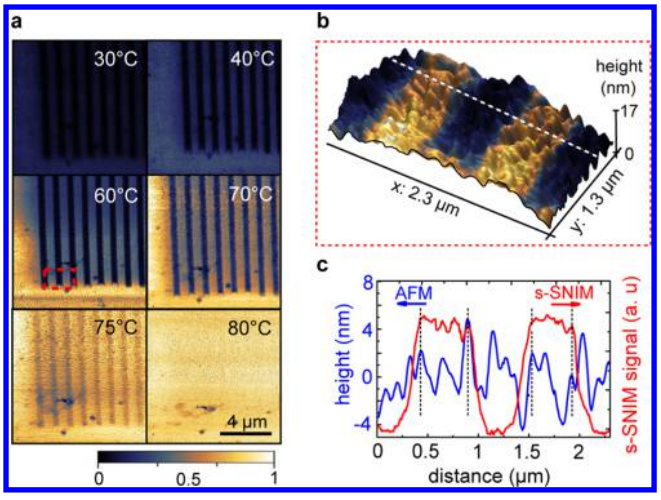

Figure 5. Limits of spatially selective defect engineering probed by infrared nanoimaging. (a) Near-field scattering amplitude of the switchable polarizer of the type shown in Figures 1b and 4 obtained by scattering-type scanning near field infrared microscopy (s-SNIM) at λ = 10.9 μm for increasing sample temperature. The scattering amplitude is related to the local value of the dielectric function and thus yields a good contrast between the insulating and metallic phases of VO_2. The contrast in the image is highest at intermediate temperatures (~60 °C), at which half of the stripes have transitioned to the metallic state while the others have not. (b) The topography of the sample measured by AFM [zoom-in, corresponding to the red dashed area in (a)] overlaid with the color map of the near-field scattering amplitude that was measured simultaneously at 60 °C. (c) Line scan of the AFM topography (blue) and near-field amplitude (red) taken at the line indicated in (b).

temperatures clearly show that the effective optical properties originate from the artificial phase coexistence and are not simply caused by a homogeneous distribution of diffused irradiation defects or long-range stress. Near-field images were obtained at temperatures from 30 to 80 °C using a scattering scanning near-field infrared microscope (s-SNIM) at a wavelength of 10.9 μm and with a spatial resolution of ~10 nm (Figure 5a). The s-SNIM signal is related to the local value of the dielectric function of the sample and provides contrast between the insulating and metallic phase.[12]

At low temperatures, both the irradiated and intrinsic VO_2 regions are in their insulating states (e.g., Figure 5a, 30 °C). As a consequence of different defect densities, the intrinsic regions appear slightly darker. With increasing temperature, the irradiated VO_2 undergoes the IMT first and thus those regions appear brighter. For increasing temperature above 60 °C, the contrast decreases and vanishes completely at >80 °C, which is in agreement with the reflectance measurements in Figure 4b,c. By comparing the near-field images with simultaneously acquired topography information, we observe that the spatial boundary between metallic (irradiated) and insulating (intrinsic) VO_2 is not sharp but follows the domain boundaries. A combined atomic force microscopy (AFM) and s-SNIM image of a film at 60 °C is shown in Figure 5b and a representative line scan through the ridges in Figure 5c. Because strain relaxation in thin films tends to terminate at grain boundaries, the best spatial resolution that can be achieved with our approach is reached when the domain size is on the order of the lateral straggle of ions in the film plane (~15 nm, see Supporting Information S2).

Correlated phase-transition materials featuring insulator-to-metal transitions such as vanadium dioxide have a promising future as tunable components in optics and optoelectronics. The introduction of defect engineering as a robust method to engineer the phase transition on a subwavelength scale greatly expands the utility of these materials, enabling new types of optical meta-devices. We envision defect engineering as a way to bring the critical transition temperature of other phase-transition materials, such as rare earth nickelates, closer to room temperature, creating an ecosystem of defect-engineered tunable optical (meta)materials for applications such as optical switching, adaptive optics, and tunable thermal emission.

■ ASSOCIATED CONTENT

Supporting Information

The Supporting Information is available free of charge on the ACS Publications website at DOI: 10.1021/acs.nanolett.5b04122.

Detailed description of the experimental methods. (PDF)

Additional information about the initial sample quality, effect of ion irradiation, optical calculations, and thermal stability of the samples. (PDF)

■ AUTHOR INFORMATION

Corresponding Authors

*E-mail: jura.rensberg@uni-jena.de.

*E-mail: mkats@wisc.edu.

Author Contributions

J.R. and S.Z. contributed equally.

Notes

The authors declare no competing financial interest.

■ ACKNOWLEDGMENTS

We thank A. Kildishev for helpful comments. This work has been partially financed by the Initiative and Networking Fund of German Helmholtz Association, Helmholtz Virtual Institute VH-VI-422 MEMRIOX, DAAD program 57051746, ARO through Grant W911NF-14-1-0669, AFOSR through Grant FA9550-12-0189, and by Draper Laboratory: SC001-

DOI: 10.1021/acs.nanolett.5b04122
Nano Lett. 2016, 16, 1050−1055

0000000731. S.Z. acknowledges support from the Singapore A*STAR National Science Graduate Scholarship. D.N.B. is the Moore Foundation Investigator in quantum materials, Grant GBMF4533. The fabrication and some of the measurements were performed at the Center for Nanoscale Systems (CNS) at Harvard University, a member of the National Nanotechnology Infrastructure Network (NNIN). Work at UCSD is supported through Grant ARO w911NF-13-1-0210.

REFERENCES

(1) Smith, D. R.; Pendry, J. B.; Wiltshire, M. C. K. *Science* **2004**, *305*, 788−792 and references therein..
(2) Chen, H.-T.; Padilla, W. J.; Zide, J. M. O.; Gossard, A. C.; Taylor, A. J.; Averitt, R. D. *Nature* **2006**, *444*, 597−600.
(3) Zheludev, N. I.; Kiversushar, Y. S. *Nat. Mater.* **2012**, *11*, 917−924 and references therein..
(4) Ou, J. Y.; Plum, E.; Zhang, J.; Zheludev, N. I. *Nat. Nanotechnol.* **2013**, *8*, 252−255.
(5) Yu, N.; Capasso, F. *Nat. Mater.* **2014**, *13*, 139−150.
(6) Zhao, Q.; Kang, L.; Du, B.; Li, B.; Zhou, K.; Tang, H.; Liang, X.; Zhang, B. *Appl. Phys. Lett.* **2007**, *90*, 011112.
(7) Werner, D. H.; Kwon, D.-H.; Khoo, I.-C.; Kildishev, A. V.; Shalaev, V. M. *Opt. Express* **2007**, *15*, 3342−3347.
(8) Yao, Y.; Shankar, R.; Kats, M. A.; Song, Y.; Kong, J.; Loncar, M.; Capasso, F. *Nano Lett.* **2014**, *14*, 6526−6532.
(9) Imada, M.; Fukimori, A.; Tokura, Y. *Rev. Mod. Phys.* **1998**, *70*, 1039−1263.
(10) Driscoll, T.; Kim, H.-T.; Chae, B.-G.; Kim, B.-J.; Lee, Y.-W.; Jokerst, N. M.; Palit, S.; Smith, D. R.; Ventra, M. D.; Basov, D. N. *Science* **2009**, *325*, 1518−1521.
(11) Liu, M.; Hwang, H. Y.; Tao, H.; Strikwerda, A. C.; Fan, K.; Keiser, G. R.; Sternbach, A. J.; West, K. G.; Kittiwatanakul, S.; Lu, J.; Wolf, S. A.; Omenetto, F. G.; Zhang, X.; Nelson, K. A.; Averitt, R. D. *Nature* **2012**, *487*, 345−348.
(12) Hosseini, P.; Wright, D.; Bhaskaran, H. *Nature* **2014**, *511*, 206−211.
(13) Tittl, A.; Michel, A.-K. U.; Schäferling, M.; Yin, X.; Gholipour, B.; Cui, L.; Wuttig, M.; Taubner, T.; Neubrech, F.; Giessen, H. *Adv. Mater.* **2015**, *27*, 4597−4603.
(14) Yin, X.; Schäferling, M.; Michel, A.-K. U.; Tittl, A.; Wuttig, M.; Taubner, T.; Giessen, H. *Nano Lett.* **2015**, *15*, 4255−4260.
(15) Qazilbash, M. M.; Brehm, M.; Chae, B.-G.; Ho, P.-C.; Andreev, G. O.; Kim, B.-J.; Yun, S. J.; Balatsky, A. V.; Maple, M. B.; Keilmann, F.; Kim, H.-T.; Basov, D. N. *Science* **2007**, *318*, 1750−1753.
(16) Yang, Z.; Ko, C.; Ramanathan, S. *Annu. Rev. Mater. Res.* **2011**, *41*, 337−367.
(17) Ladd, L. A.; Paul, W. *Solid State Commun.* **1969**, *7*, 425−428.
(18) Jaramillo, R.; Ha, S. D.; Silevitch, D. M.; Ramanathan, S. *Nat. Phys.* **2014**, *10*, 304−307.
(19) Sheik-Bahae, M.; Hagan, D. J.; Van Stryland, E. W. *Phys. Rev. Lett.* **1990**, *65*, 96−99.
(20) Humar, M.; Ravnik, M.; Pajk, S.; Muševič, I. *Nat. Photonics* **2009**, *3*, 595−600.
(21) Kats, M. A.; Blanchard, R.; Genevet, P.; Yang, Z.; Qazilbash, M. M.; Basov, D. N.; Ramanathan, S.; Capasso, F. *Opt. Lett.* **2013**, *38*, 368−370.
(22) Townsend, P. D.; Chandler, P. J.; Zhang, L. *Optical Effects of Ion Implantation*; Cambridge University Press: New York, 1994.
(23) Shibuya, K.; Kawasaki, M.; Tokura, Y. *Appl. Phys. Lett.* **2010**, *96*, 022102.
(24) Kübler, C.; Ehrke, H.; Huber, R.; Lopez, R.; Halabica, A.; Haglund, R. F.; Leitenstorfer, A. *Phys. Rev. Lett.* **2007**, *99*, 116401.
(25) Jeong, J.; Aetukuri, N.; Graf, T.; Schladt, T. D.; Samant, M. G.; Parkin, S. S. P. *Science* **2013**, *339*, 1402−1405.
(26) Appavoo, K.; Lei, D. Y.; Sonnefraud, Y.; Wang, B.; Pantelides, S. T.; Maier, S. A.; Haglund, R. F., Jr. *Nano Lett.* **2012**, *12*, 780−786.
(27) Cao, J.; Ertekin, E.; Srinivasan, V.; Fan, W.; Huang, S.; Zhang, H.; Yim, J. W. L.; Khanal, D. R.; Ogeltree, D. F.; Grossman, J. C.; Wu, J. *Nat. Nanotechnol.* **2009**, *4*, 732−737.
(28) Park, J. H.; Coy, J. M.; Kasirga, T. S.; Huang, C.; Fei, Z.; Hunter, S.; Cobden, D. H. *Nature* **2013**, *500*, 431−434.
(29) Aetukuri, N. B.; Gray, A. X.; Drouard, M.; Cossale, M.; Gao, L.; Reid, A. H.; Kukreja, R.; Ohldag, H.; Jenkins, C. A.; Arenholz, E.; Roche, K. P.; Dürr, H. A.; Samant, M. G.; Parkin, S. S. P. *Nat. Phys.* **2013**, *9*, 661.
(30) Brokate, M.; Sprekels, J. *Hysteresis and Phase Transitions*; Springer: New York, 1996.
(31) Zhao, L.; Miao, L.; Liu, C.; Li, C.; Asaka, T.; Kang, Y.; Iwamato, Y.; Tanemura, S.; Gu, H.; Su, H. *Sci. Rep.* **2014**, *4*, 7000.
(32) Wesch, W.; Wendler, E.; Schnohr, C. S. *Nucl. Instrum. Methods Phys. Res., Sect. B* **2012**, *277*, 58−69.
(33) Hofsäss, H.; Ehrhardt, P.; Gehrke, H.-G.; Brötzmann, M.; Vetter, U.; Zhang, K.; Krauser, J.; Trautmann, C.; Ko, C.; Ramanathan, S. *AIP Adv.* **2011**, *1*, 032168.
(34) Ufert, K. D.; Terukov, E. I. *Phys. Stat. Sol. A* **1977**, *40*, K157.
(35) Kats, M. A.; Sharma, D.; Lin, J.; Genevet, P.; Blanchard, R.; Yang, Z.; Qazilbash, M. M.; Basov, D. N.; Ramanathan, S.; Capasso, F. *Appl. Phys. Lett.* **2012**, *101*, 221101.
(36) Kats, M. A.; Blanchard, R.; Zhang, S.; Genevet, P.; Ko, C.; Ramanathan, S.; Capasso, F. *Phys. Rev. X* **2013**, *3*, 041004.
(37) Chen, Y. G.; Kao, T. S.; Ng, B.; Li, X.; Luo, X. G.; Luk'yanchuk, B.; Maier, S. A.; Hong, M. H. *Opt. Express* **2013**, *21*, 13691−13698.
(38) Paik, T.; Hong, S.-H.; Gaulding, E. A.; Caglayan, H.; Gordon, T. R.; Engheta, N.; Kagan, C. R.; Murray, C. B. *ACS Nano* **2014**, *8*, 797−806.
(39) Liu, M.; Sternbach, A. J.; Wagner, M.; Slusar, T. V.; Kong, T.; Bud'ko, S. L.; Kittiwatanakul, S.; Qazilbash, M. M.; McLeod, A.; Fei, Z.; Abreu, E.; Zhang, J.; Goldflam, M.; Dai, S.; Ni, G.-X.; Lu, J.; Bechtel, H. A.; Martin, M. C.; Raschke, M. B.; Averitt, R. D.; Wolf, S. A.; Kim, H.-T.; Canfield, P. C.; Basov, D. N. *Phys. Rev. B: Condens. Matter Mater. Phys.* **2015**, *91*, 245155.
(40) Jostmeier, T.; Zimmer, J.; Karl, H.; Krenner, H. J.; Betz, M. *Appl. Phys. Lett.* **2014**, *105*, 071107.
(41) Können, G. P. *Polarized Light in Nature*; Cambridge University Press: New York, 1985.
(42) Lalanne, P., Hutley, M. *Artificial Media Optical Properties - Subwavelength Scale*; Encyclopedia of Optical Engineering; Dekker: New York, 2007.
(43) Soref, R. A.; Bennet, B. R. *IEEE J. Quantum Electron.* **1987**, *23*, 123−129.

DOI: 10.1021/acs.nanolett.5b04122
Nano Lett. 2016, 16, 1050−1055